

An integrated ion trap for the photon-ion spectrometer at PETRA III

Cite as: Rev. Sci. Instrum. **94**, 023201 (2023); <https://doi.org/10.1063/5.0111097>

Submitted: 18 July 2022 • Accepted: 22 January 2023 • Published Online: 09 February 2023

 S. Reinwardt,  I. Baev,  F. Linß, et al.



View Online



Export Citation



CrossMark

ARTICLES YOU MAY BE INTERESTED IN

[Concurrent surface enhanced infrared and Raman spectroscopy with single molecule sensitivity](#)

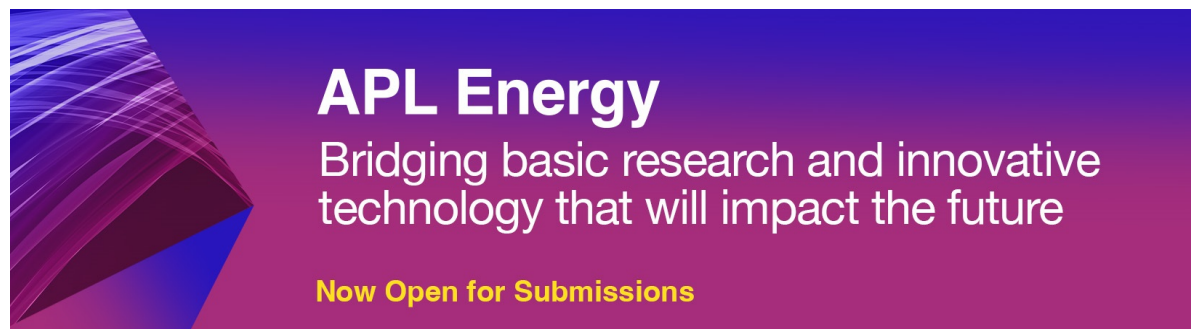
Review of Scientific Instruments **94**, 025103 (2023); <https://doi.org/10.1063/5.0136908>

[Post collision analyzer to study charge-exchange processes in ion-molecule collisions](#)

Review of Scientific Instruments **93**, 113306 (2022); <https://doi.org/10.1063/5.0121351>

[Neutron imaging of inertial confinement fusion implosions](#)

Review of Scientific Instruments **94**, 021101 (2023); <https://doi.org/10.1063/5.0124074>



APL Energy
Bridging basic research and innovative
technology that will impact the future
Now Open for Submissions

An integrated ion trap for the photon-ion spectrometer at PETRA III

Cite as: *Rev. Sci. Instrum.* **94**, 023201 (2023); doi: 10.1063/5.0111097

Submitted: 18 July 2022 • Accepted: 22 January 2023 •

Published Online: 9 February 2023



View Online



Export Citation



CrossMark

S. Reinwardt,¹ I. Baev,¹ F. Linß,¹ P. Cieslik,¹ O. Raberg,¹ T. Buhr,² A. Perry-Sassmannshausen,² S. Schippers,² A. Müller,² F. Trinter,^{3,4} A. Guda,⁵ R. Laasch,⁶ and M. Martins^{1,a)}

AFFILIATIONS

¹Institut für Experimentalphysik, Universität Hamburg, Luruper Chaussee 149, 22761 Hamburg, Germany

²I. Physikalisches Institut, Justus-Liebig-Universität Gießen, Heinrich-Buff-Ring 16, 35392 Giessen, Germany

³Institut für Kernphysik, Goethe-Universität Frankfurt, Max-von-Laue-Straße 1, 60438 Frankfurt am Main, Germany

⁴Molecular Physics, Fritz-Haber-Institut der Max-Planck-Gesellschaft, Faradayweg 4-6, 14195 Berlin, Germany

⁵The Smart Materials Research Institute, Southern Federal University, Sladkova 178/24, 344090 Rostov-on-Don, Russia

⁶Brookhaven National Laboratory, 98 Rochester St, Upton, New York 11973, USA

^{a)}Author to whom correspondence should be addressed: michael.martins@uni-hamburg.de

ABSTRACT

We have added a multipole ion trap to the existing photon-ion spectrometer at PETRA III (PIPE). Its hybrid structure combines a ring-electrode trap with a segmented 16-pole trap. The interaction of gases and ions with extreme ultraviolet radiation from the beamline P04 is planned to be investigated with the newly installed multipole trap. The research focus lies on radiation-induced chemical reactions that take place in the interstellar medium or in the atmospheres of planets, including natural as well as man-made processes that are important in the Earth's atmosphere. In order to determine the mass-to-charge ratio of the stored ions as efficiently as possible, we are using an ion time-of-flight spectrometer. With this technique, all stored ions can be detected simultaneously. To demonstrate the possibilities of the trap setup, two experiments have been carried out: The photoionization of xenon and the ion-impact ionization of norbornadiene. This type of ion-impact ionization can, in principle, also take place in planetary atmospheres. In addition to ionization by photon or ion impact, chemical reactions of the trapped ions with neutral atoms or molecules in the gas phase have been observed. The operation of the trap enables us to simulate conditions similar to those in the ionosphere.

Published under an exclusive license by AIP Publishing. <https://doi.org/10.1063/5.0111097>

I. INTRODUCTION

The photon-matter interaction is one of the most important processes in nature. Various valuable methods that use this process to study the properties of matter ranging from isolated atoms to molecules, clusters, and solid-state samples have been developed.^{1,2}

In particular, x-ray photons from highly brilliant synchrotron-radiation sources offer very powerful methods, such as near-edge x-ray absorption fine-structure spectroscopy (NEXAFS) due to their element and site specificity. Linked to the development of advanced instruments, NEXAFS has become possible also on charged particles. These charged particles open an avenue for a wide range of highly interesting target systems hardly accessible or even inaccessible with neutrals such as molecular ions,³⁻⁵ ionic radicals,⁶ mass-selected clusters,⁷ and astrophysically relevant molecules.⁸

To investigate charged particles using synchrotron radiation, two methods have been established to overcome the very low target density of ionic targets, namely, the ion-photon merged-beams technique⁹⁻¹¹ and ion traps.^{3,12} The merged-beams technique is realized at the photon-ion spectrometer instrument at PETRA III (PIPE) at DESY in Hamburg, Germany.^{13,14} It has been successfully used to measure absolute and partial photoionization cross sections of atomic ions in the range of several hundreds of Mb¹⁵ down to $(2 \pm 1)b$,¹⁶ to record x-ray absorption spectra of molecular ions,¹⁷ and to study ultrafast dissociation processes in small molecular ions.⁶ In this technique, the ion and photon beams are merged collinearly over a distance of the order of 1 m, thereby increasing the interaction volume.

Compared to the merged-beams technique, longer exposure times can be achieved with an ion trap, where a large number of

ions ranging from atoms to small nanoparticles can be stored in a well-defined volume, taking into account the boundary of the space charge. This enables capturing and detecting photoions and, therefore, the investigation of complex photoexcitation processes with soft x rays. Such studies have been performed at free-electron lasers,^{18,19} as well as at synchrotron-radiation facilities.^{3,12} Ion traps are also widely used to investigate ion-atom/ion-molecule collisions or chemical reactions^{20–22} relevant, e.g., in planetary atmospheres or in interstellar and intergalactic media. For example, to simulate collisions of molecular ions in Earth's atmosphere in the laboratory,²³ ion traps have been proven to be an ideal laboratory solution, e.g., for studying collisions with volatile organic compounds²⁰ or with inorganic compounds such as ozone.²⁴

In this paper, we present a radio-frequency (RF) ion trap integrated in the PIPE instrument at PETRA III (DESY). Figure 1 shows the complete setup with the new ion trap. The trap can use the PIPE ion beamline as an injector to study photoionization processes of stored ions or neutral gases, as well as neutral gas-ion collision processes. Furthermore, chemical reactions of neutral gases following a photoexcitation can be investigated. We describe the design of the ion trap and its integration into the PIPE setup, as well as proof-of-principle experiments in different operation modes of the trap.

II. EXPERIMENTAL DESIGN

The RF ion-trap setup is a part of the stationary photon-ion spectrometer setup at the synchrotron light source “PETRA III” (PIPE).^{13,14} The PIPE setup has been developed for the transport of keV ion beams to the interaction regions. The ion trap can be used to trap mass-over-charge-selected ions from the PIPE ion beamline. For this, the ions are decelerated by applying a potential of

up to 2000 V to the trap and loaded into the trap, where their interaction with the extreme ultraviolet (XUV) photons from the PETRA III beamline P04²⁵ can be studied. It is also possible to pass the ions through the trap with a higher kinetic energy in order to ionize neutral gases as target material.

A. Ion-trap geometry and RF stabilization

The ion trap is a hybrid structure, which consists of a ring-electrode trap^{27,28} and a segmented 16-pole trap.²⁹ By using a segmented trap with 34 parts, it is possible to create an effective trap length of more than 180 mm so that a very large interaction region is provided. The segmentation of the trap enables the generation of potential gradients along the trap, which can be used to improve the extraction of the ions. An extraction from a simple multipole trap would be significantly more difficult due to the trap length. The development of the segmented geometry allows the combination of large trap lengths and multipole geometries. A multipole trap with a large trapping volume and an associated low probability of ion-ion collisions²⁹ is a versatile solution for collecting photoions because the product channels often have very different mass-to-charge ratios. With the employed trap geometry, it is possible to accumulate photoions over large mass-over-charge ranges from few *u* to 1000 *u*, which has been proven with C₆₀⁺ cations. Trapping of even larger ions with larger masses of several 1000 *u* should be possible. Thus, heavy and light ions can be trapped in parallel in the same field and at the same time.

The individual trap segments are made by wire erosion of two interleaved copper plates with eight electrode structures each [Fig. 2(a)]. Due to the geometry of the intersecting copper plates, the stored ions only experience the inner 16-electrode field. To configure a ring-electrode trap,²⁷ it is possible to electrically connect the copper plates of one segment and, thereby, create a ring electrode.

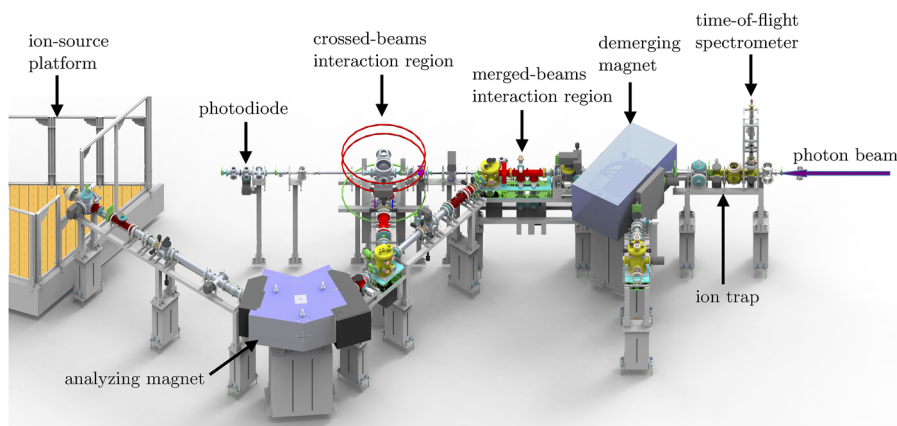


FIG. 1. The permanently installed photon-ion end-station PIPE at the XUV beamline P04²⁵ at PETRA III for studying interactions of photons with atomic and molecular ions, as well as small, charged nanoparticles. The setup consists of three interaction regions: a crossed-beams interaction region, a merged-beams interaction region, and the newly integrated ion trap. The photon beam enters the setup from the right and passes through the three interaction regions. At the end of the photon beamline, we have installed a calibrated photodiode, with which the photon flux can be continuously monitored.²⁶ The ion beams are generated in an ion source mounted on the ion-source platform at the left. The analyzing magnet enables a selection of ions according to their mass-to-charge ratio for further beam transfer to the interaction regions. Electrostatic deflectors allow the ion beam to be directed either to the crossed-beams or to the merged-beams region. The demerging magnet is used in merged-beams experiments to separate photoions from the primary ion beam. In order to route the ion beam to the trap, the demerging magnetic field was set to 0 G. To achieve this, the remanence of the magnet was compensated by a small reverse current in the magnet coils. Details of the setup are described in Refs. 13 and 26.

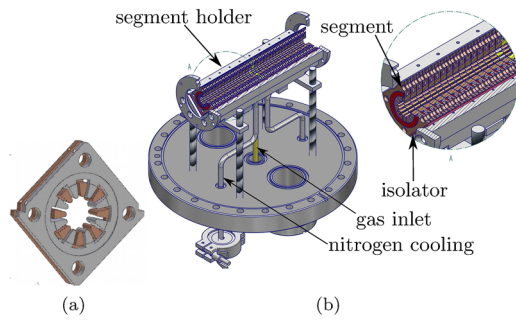


FIG. 2. The segmented ion trap of the PIPE setup located at the XUV beamline P04 at synchrotron PETRA III. (a) One 16-pole trap²⁹ segment consists of two interleaved copper plates, one of which is shown with gray shading, while the other one is copper-colored. The gray plate and the copper-colored plate are electrically isolated from each other by a polyether ether ketone (PEEK) ring. The radio-frequency field is applied to the two electrodes. (b) The trap holder houses in total 34 trap segments, which are electrically isolated from each other by sapphire plates. Furthermore, the holder has a coolant inlet and a gas inlet. Similar to a ring-pole trap,^{27,28} the radio frequency is applied between the neighboring copper plates. The trap, with a length of 200 mm, offers a comparatively large volume. This is advantageous for experiments with a photon beam directed along the trap axis.

In total, 34 segments are placed in a segment holder [Fig. 2(b)]. The inner diameter of the ion trap is 10 mm, and the electrode curvature radius is 0.7 mm. These values fulfill the relation for the 16-pole potential approximation.³⁰ Within the trap, the photon-beam has a size of $\sim 0.6 \times 1.6 \text{ mm}^2$ (horizontal \times vertical), depending on the monochromator exit-slit width (the vertical beam size is given for an exit-slit width of 1000 μm here). The exact photon-beam position varies slightly with the electron-beam position in the PETRA III storage ring and the settings of the photon beamline P04. The given ratio of photon beam size and trap diameter ensures that the photon beam can always pass through the trap.

To describe the effect of the electrode geometry on the trapped ions, we have solved the Laplace equation using the finite-element method as implemented in the SIMION code.³¹ In a second step, we have evaluated over 100 ion trajectories in the ion trap by numerical integration, assuming suitable initial conditions for the ions from the PIPE ion beamline. The RF potential of the ion trap was described by a sine function with a frequency of 3 MHz and an amplitude of 20 V. Adapted to the PIPE injection parameters, a source-size distribution of 3 mm and a size-cone-direction distribution with a half angle of 3° were applied. The simulations have been performed for four different fixed injection energies, as given in Fig. 3(c). Subsequently, transverse projections of the ion-density distributions within the trap were calculated from the trajectory points of the numerical integration. Around one billion points of the trajectories were evaluated in order to obtain a two-dimensional ion density map, as shown in Fig. 3(a). The thus computed pattern reflects the 16-electrode trap structure. Furthermore, the numerical calculations show that the ion-density in the area between the poles is reduced when hyperbolically shaped electrodes are used, compared to a multipole trap consisting of simple rods. The ion-density distribution in the trap approximately corresponds to a circular geometry. The radial distribution of the ion-density in the trap was determined

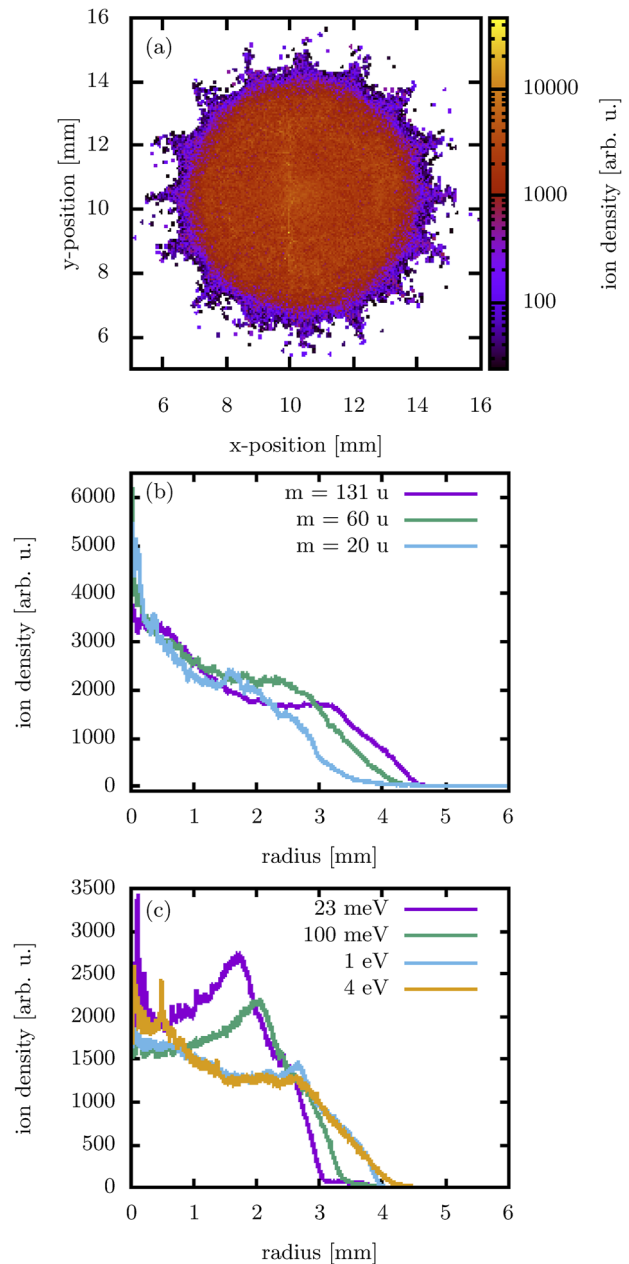


FIG. 3. The ion density of our 16-pole trap calculated from the ion trajectories simulated with SIMION. In panel (a), the radial ion-distribution for ions with a mass-to-charge ratio of 60 ue^{-1} and a kinetic energy of 4 eV is shown in the projection of the trap inventory onto the trap axis. In panel (b), the radial ion densities for different masses are shown. In panel (c), the radial ion densities for different initial energies along the axis of the ion trap are shown. A mass-over-charge ratio of 60 ue^{-1} was assumed again.

from the two-dimensional ion-density map. using a radial grid that was placed over this ion-density map. Figure 3(b) shows a relatively even ion-distribution inside the trap, with an increase toward the central trap axis. Due to the different masses, the particles are

subject to different effective potentials, which means that the particles with a higher mass can penetrate more deeply into the RF potential barrier. Between radii of 3 and 4.5 mm, the ion density is decreasing [Fig. 3(b)]. Due to the very small area in which the ions are deflected back toward the trap axis, the influence of the RF field on the trajectories is reduced. Therefore, the mass-over-charge range, for which trapping is possible, is increased.

Figure 3(c) shows the change in radial distribution with axial start energy. The particles initially move along the trap with a velocity corresponding to the axial start energy. The radial plot clearly shows that ions with higher kinetic energy fly further outward. The 23 meV curve has a maximum in the ion density at 1.5 mm. When comparing the curves, it can be seen that this maximum is shifted to larger radii at higher kinetic energies and that the maximum flattens out significantly. In Table I, the mean radial kinetic energies of the ions are shown. Those result from the velocity of the ions in the direction of the radio-frequency potential. It can be seen that the radial energy of the ions increases with higher starting energy. The energies should be as low as possible; otherwise, the ions cannot be trapped under the applied radio-frequency parameters. The simulated particles with a mass-over-charge ratio of 60 ue^{-1} experience an effective potential of 0.27 eV at a reduced radius \hat{r} of 0.9, which takes into account the assumption that there should be some free space between the maximum transverse elongation of the ions and the electrodes. The trapping properties in multipole traps, described in the adiabatic theory by Gerlich using the stability parameter, must be below 0.3 for stable trapping.^{20,32} From Gerlich's theory [see Eq. (24) of Ref. 32], it follows that the stability parameter in the radial turning point can be described by

$$\eta = \frac{2(n-1)}{\pi f r_0 \hat{r}} \sqrt{\frac{E}{m_{\text{ion}}}}, \quad (1)$$

where f is the frequency of the radio-frequency potential. r_0 is the radius of the ion trap. E is the radial energy of the ion. n is the number of rod pairs. \hat{r} was also chosen as 0.9. From the stability parameters listed in Table I, it can be seen that the investigated ions with different kinetic energies can be trapped stably.

In addition to the transverse trapping properties, the segmented structure enables us to apply a longitudinal gradient, which is used for a more efficient longitudinal ion extraction. The copper plates of one RF phase are connected via a voltage divider, and the copper plates of the opposite RF phase are connected via a second voltage

TABLE I. The mean radial kinetic energies of the trajectories shown in Fig. 3(c). For these trajectories, a mass-over-charge ratio of 60 ue^{-1} was assumed. The radial energy results from the ion velocity with which they fly into the radio-frequency potential. The adiabatic stability parameter was calculated from the mean radial energy.

Axial start energy	Mean radial energy	Stability parameter
23 meV	1 meV	0.01
100 meV	4 meV	0.03
1 eV	0.11 eV	0.14
4 eV	0.23 eV	0.20

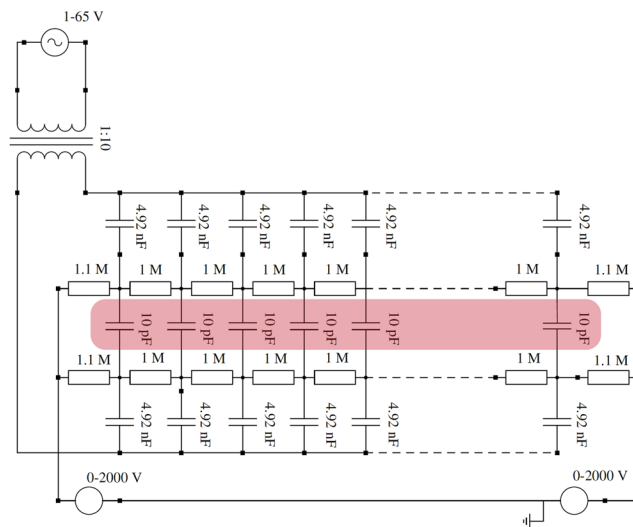


FIG. 4. The wiring of the individual trap elements with the voltage dividers and the coupling capacitors. The capacitors marked by red color represent the trap elements. The active amplifier for the oscillator is connected to the transformer. The active amplifier for the oscillator and the transformer are installed in the generator. Since the transformer is a fundamental part of the oscillating circuit, it was drawn separately in this figure.

divider. At the voltage dividers, a potential gradient of up to 300 mV per segment can be applied, and the trap can be raised up to a potential of 2000 V to decelerate the ions from the keV ion-beam. A potential of 1000 V and a gradient of 63 mV per segment were used in the experiments presented here. The RF coupling to the copper segments is realized by capacitors on two printed circuit boards that are screwed directly onto the trap. Electrical capacitors are connected in parallel to the voltage divider (see Fig. 4). The capacitors have a much higher capacitance than the trap segment itself. This ensures that only the trap segments' capacity influences the resulting frequency of the ion trap. With the help of an RF generator, which was specially developed by CGC instruments, 09112 Chemnitz, Germany, and works according to the principle of a radio-frequency power supply, as described in Ref. 33, a radio frequency of 3 MHz was employed with an amplitude of 18 V, which was sufficient for capturing the ions. The generator has two monitor outputs, which were used to check the radio frequency on the trap with an oscilloscope. Only for heavy ions such as C_{60}^+ , with a mass of 720 u, was it necessary to increase the radio-frequency amplitude to 80 V. This corresponds to an effective potential of 0.35 eV at a reduced radius of 0.9.

B. Timing of trapping, extraction, and time-of-flight measurement

A schematic trajectory of the ions through the setup is illustrated in Fig. 5. For measuring the ions' time of flight after opening the trap via the pulsed outlet cap PC II, a portion of the ions is extracted, focused by the after-trap lens (ATL) (typical voltages for the three cylinders of the lens are $\text{ATL1} = 100 \text{ V}$, $\text{ATL2} = 1250 \text{ V}$,

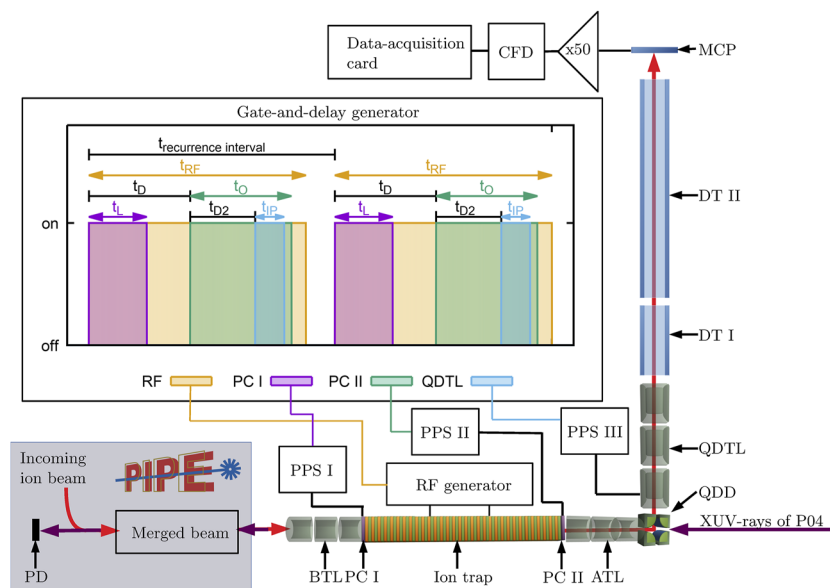


FIG. 5. Schematic setup for measurements with the ion trap. A schematic trajectory from the ion trap to the time-of-flight spectrometer is illustrated by the red arrows. The ions can be generated directly in the trap or injected into the trap from the ion beamline. The before-trap lens (BTL) is used for deceleration and focusing of the ions. With the pulsed end caps, PC I and PC II of the trap, the ions are trapped in the axial direction. After a certain exposure time, given by the delay time t_D between the opening of PC I and PC II, the ions are extracted with a kinetic energy of 1 keV by the after-trap lens (ATL). The electrostatic quadrupole deflector (QDD) and the quadrupole-triplet lens (QDTL) direct the trapped ions to the time-of-flight spectrometer to determine their mass-to-charge ratio. The photon beam represented by the purple arrow enters the experiment from the right. The time-of-flight spectrometer consists of the drift tubes DT I and DT II and a Chevron stack of microchannel plates (MCP) with an active diameter of 20 mm. The photon flux is permanently monitored by the calibrated photodiode (PD).

and ATL3 = 600 V), and deflected toward the time-of-flight spectrometer by the electrostatic quadrupole deflector (QDD). A negative and a corresponding positive voltage of 1250 V is usually applied to the elements for the deflection. Before reaching the drift tubes “DT I” and DT II, the ions are refocused by the quadrupole-triplet lens (QDTL). One electrode of the QDTL is used to cut out a part of the ion bunch that was generated using the extraction via PC II. The resulting very sharp ion pulse, with a typical pulse width $t_{IP} = 1.6 \mu\text{s}$, is then passed through the drift tubes of the ion time-of-flight spectrometer. This pulse width creates a selection of about 10% of the extracted ions. The flight time of the ions to the microchannel plate (MCP) detector depends on the mass of the ions, which allows us to record a mass spectra of ions produced or manipulated inside the ion trap.

During the neutral-gas ionization, the trap entrance side remains closed by an electrostatic potential on the ion-inlet pulsed cap PC I. Upon opening of PC I, ions from the permanently installed ion beamline can be injected into the radio-frequency potential of the trap. With the ion beamline, there is also the possibility of passing ions with a higher kinetic energy through the trap. This allows the kinetic energy of the ions to be set for ion-impact experiments. At higher kinetic energies, these ions cannot be trapped in the trap potential any longer.

In Fig. 5, the schematic connection of the components for a measurement and the time control are shown. To synchronize the quadrupole-triplet electrode with PC I, PC II, and the radio-frequency generator, a gate-and-delay generator 9520 from Quantum

Composers Inc., Bozeman, MT 59718, USA, is used in the setup. The RF generator is switched off between the cycles so that no ions from a preceding cycle remain in the trap. By successively changing the delay time t_D between opening PC I and PC II, the development of the ion intensity over time can be determined. If t_D is shorter than the opening time t_L of PC I, the charging with the primary ion beam from the ion beamline or the increase in the ion intensity by ion-impact ionization can be investigated. If t_D is longer than t_L , the trapping time of ions generated by either photoionization or ion-impact ionization can be studied. 20 μs after the ion trap has been opened at PC II for the time $t_O = 30 \mu\text{s}$, the start pulse for the time-of-flight measurement is generated by lowering the potential on one of the electrodes of the quadrupole triplet for typically $t_{IP} = 1.6 \mu\text{s}$ from 110 to 10 V is the right potential to route the ions into the spectrometer, and 110 V is the potential to deflect and defocus the ions so that they cannot enter the spectrometer. The other elements of the QDTL usually have a voltage varying from -50 to 50 V.

In order to guarantee a well-defined timing, the potentials at PC I, PC II, and the variable-potential electrode of the QDTL were controlled by three Si-MOSFET push-pull switches (PPS) from the GHTS series produced by Behlke Power Electronics GmbH, 61476 Kronberg im Taunus, Germany. The input voltages of the PPS were stabilized by capacitors, which have a much higher capacity than the associated ion-optical element. This way, PC I and PC II can be opened precisely for the times t_L and t_O .

If the delay t_{D2} between the opening of the ion trap and the pulsing of the quadrupole triplet is further reduced, stored ions with

a higher kinetic energy are detected in the time-of-flight spectrometer. A typical value for this delay is 20 μs . When choosing longer delays, stored ions with a lower kinetic energy are routed to the time-of-flight spectrometer. The width of the kinetic-energy distribution can be adjusted with the pulse time t_{IP} of the quadrupole triplet. Shorter pulses lead to a higher resolution in the kinetic energy. The time-of-flight spectrometer contains a short drift tube (DT I) of 300 mm and a long drift tube (DT II) of 700 mm. A typical voltage for DT I is 600 V, and a typical voltage for DT II is 100 V. This results in a total drift length of 1000 mm. The separation into two drift sections increases the degree of freedom for temporal focusing of the ions. Thereby, the spectrometer provides the possibility to be used at a certain high-resolution mass-over-charge range. The ion signal is amplified by using a stack of microchannel plates (MCPs) from tectra GmbH, 60323 Frankfurt, Germany. The MCP signal is amplified by the broadband amplifier 6954 from Philips Scientific, Mahwah, NJ 07430, USA, processed by the constant-fraction discriminator (CFD) 934 from ORTEC, Oak Ridge, TN 37830, USA, and recorded with the 10 bit analog-to-digital converter module U1065A from Agilent Technologies, Santa Clara, CA 95051, USA. Approximately 250 000 traces with a sampling rate of 1 GS s^{-1} and a maximum amplitude of 2 V were summed up for a spectrum at a resulting analog-to-digital converter resolution of 1.95 mV. After each measurement, the radio frequency of the ion trap is switched off for 300 μs (see the difference between t_{RF} and $t_{\text{recurrence interval}}$ in Fig. 5) to avoid the trapped ions interfering with the next cycle. The entire measurement cycle can be carried out at a repetition rate of up to 295 Hz or a recurrence-interval time of at least 3.4 ms (Fig. 5). The times t_{L} , t_{D} , and t_{RF} must be adjusted individually to the repetition rate. When changing the repetition rate, the other times do not have to be changed. Due to the analysis via a time-of-flight spectrometer, the mass-to-charge ratio of all captured ions can be determined by only one time-of-flight measurement. This particularly efficient analysis method allows the experimenter to simultaneously record an absorption spectrum of all fragment channels in 50 μs .

III. EXPERIMENTAL SCHEMES

To demonstrate the experimental possibilities of this ion-trap setup for atomic and molecular physics, we present two possible experiments. The first experiment addresses the photoionization of neutral gases and the subsequent trapping of the ionization products. The second experiment deals with the possibility to stimulate chemical reactions. As an example for this class of experiments, a chemical reaction between an ion generated by ion-impact ionization and a neutral-gas particle is presented.

A. Photoionization and subsequent trapping

For the demonstration experiment, xenon (99.99% purity) gas was fed into the center of the trap via a gas inlet. The gas flow into the radio-frequency trap was regulated via a metering valve from Vakuum-Anlagenbau GmbH, 25337 Elmshorn, Germany. A pressure of 3.6×10^{-4} Pa was set with the metering valve, using the hot-cathode vacuum gauge of the high-vacuum chamber. An ion-gauge correction factor of 2.78 was used to correct the gas pressure.³⁴ In the ion trap, the neutral target gas can be ionized by the incoming

XUV radiation. The resulting photoions are captured by the radio-frequency potential, with an amplitude of 18 V.

The ionization of the neutral Xe atoms was carried out at the Xe $3d_{5/2}$ and $3d_{3/2}$ edges.³⁵ A summed mass spectrum over the photon-energy range 680 to 710 eV is shown in Fig. 6. The photon flux amounted to 5×10^{12} s^{-1} at a photon energy of 703 eV. The individual xenon isotopes and charge states are clearly visible in the spectrum. In order to detect the highly charged Xe^{7+} ions, the delay between the opening pulse of the trap and the quadrupole triplet t_{D2} was shifted toward shorter times, thus toward ions with a higher kinetic energy. t_{IP} was lowered from 1.3 to 0.9 μs to further improve the energy resolution and the mass resolution. The voltages applied to the drift tubes were adjusted such that ions with a very low mass-to-charge ratio could be resolved. For ions with a kinetic energy of a few meV, the resolutions for the individual Xe charge states are shown in Table II. To obtain the mass resolution, the peaks for the different isotopes were fitted by Gaussian functions. The mass resolving power $m/\Delta m$ was then determined from the peak position and the FWHM. In order to achieve the best possible resolution for higher mass-to-charge ratios, the voltages and the timing of the time-of-flight spectrometer were adjusted. Thereby, the resolution of the Xe^{4+} feature could be improved from a $m/\Delta m$ of 153 to 201. In addition to the mass resolution, the branching ratios for the different charge states are also shown in Table II. Our experimental values were obtained by integrating the isotope structures. They can be compared with those published by Saito and Suzuki, who determined the ion yield by time-of-flight spectrometry.^{36,37} Comparison of our data with the values from the literature yields good

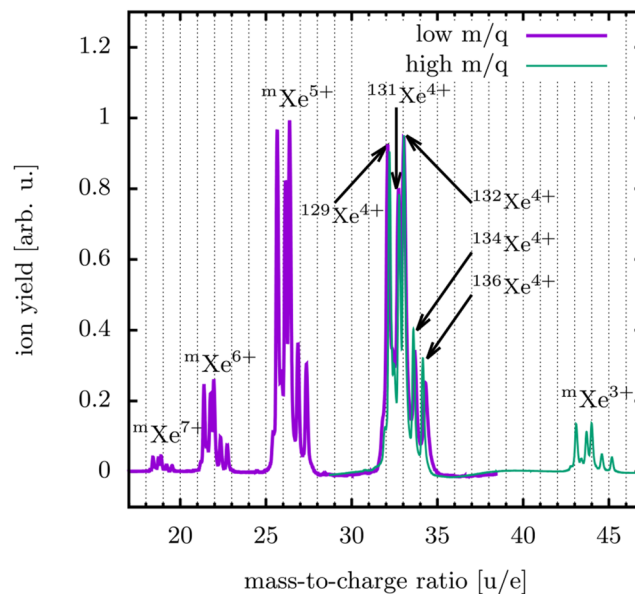


FIG. 6. The summed time-of-flight spectra of xenon ions resulting from the photoionization of neutral xenon gas in the trap over the measured photon energy range 680 to 710 eV, employing our ion trap. A first spectrum is shown for a low m/q and a second for a high m/q for the lower charge states 3+ and 4+. The isotope structure of xenon for the different charge states can be recognized very well in the time-of-flight spectrum.

TABLE II. The table shows the resolution determined from the individual peaks in Fig. 6. For each mass-to-charge peak, the resolution was determined by a Gaussian fit. Then, we averaged over the individual resolutions for a given charge state. The branching ratio was determined from the integrals of the peaks. A correction of the MCP detection efficiency for the different ions was made.³⁸ The branching ratio has a relative uncertainty of 10%. The reference branching ratio was determined by the values from Saito and Suzuki at 686 eV photon energy.³⁷ Since only five charge states were measured, the percentage values for the reference are reduced to these five charge states so that a comparison is possible.

Charge state	m/q [u/e]	m/ Δ m	Branching ratio (%)	Reference 37 (%)	MCP detection efficiency ³⁸ (%)
3	43.6	242	8.2	9.1	34.5
4	32.8	201	47.3	44.7	40.6
5	26.2	183	34.9	28.7	44.7
6	21.8	172	8.2	14.9	47.6
7	18.7	159	1.4	2.6	49.8

agreement, with the largest deviation of 6.7% in the branching ratio for Xe^{6+} . For Xe^{7+} , the error becomes significantly larger. On the one hand, this might be due to the lower trapping efficiency for smaller m/q values. On the other hand, the uncertainty becomes significantly larger due to the lower ion yield. In addition to the MCP efficiencies for the ion detection, parts of the setup, such as the ion optical elements, can also have an influence on the branching ratio. In order to investigate this influence, the mass-dependent transmission of the ion-optical elements was modeled using SIMION. A mass-independent transmission of 70% has been obtained from the simulation.

B. Ion-molecule collisions

As an example for the second class of possible experiments, results are presented for ion-impact ionization of norbornadiene, C_7H_8 , with Ar ions and subsequent chemical reactions. Possibilities of ion-molecule collision experiments, which are carried out using an ion beam from the PIPE setup, are described. For the ion-impact ionization of norbornadiene, Ar^+ and Ar^{2+} ions were used with a kinetic energy of 500 eV for Ar^+ and 1000 eV for Ar^{2+} . For these energies, the ions were accelerated in PIPE with a potential of 1.5 kV and decelerated by the 1 kV trap potential. The trap was operated at a radio-frequency amplitude of 18 V. Norbornadiene was chosen for this experiment because of its high ionization potential of 8.6 eV³⁹ and its favorable trapping properties due to its relatively high mass. Furthermore, it is a reactive substance that undergoes addition reactions, see Ref. 40 and references therein. A few ml of norbornadiene was filled into a test tube, which was directly connected to the gas inlet of the trap setup. The chemical had a purity of 97%. The remaining 3% has a chemical composition of 0.25%–1% toluene, 0.1%–1% cycloheptatriene, 0.25%–1% cyclopentadiene, and for the stabilization, a share of 0.1%–0.25% butylated hydroxytoluene. In the ion-impact experiment, the repetition rate was adjusted to 25 Hz, corresponding to a recurrence-interval time of up to 40 ms.

In Fig. 7, the ion-impact products resulting from a collision with norbornadiene and Ar^+ or Ar^{2+} are shown. Due to the collisions with Ar ions, the kinetic energy of the C_nH_m^+ ions is significantly higher than the kinetic energy of the Xe^{q+} ions produced by photoionization. As a result, the mass resolution of the norbornadiene fragments is significantly lower. A resolution of $m/\Delta m = 60$

could be determined from Gaussian fits to the C_7H_x^+ and C_9H_x^+ peaks. The kinetic energy of C_7H_x^+ was higher than the kinetic energy of C_9H_x^+ . As a result, a longer t_{IP} of 2 μs had to be chosen so that C_9H_x^+ and C_7H_x^+ could be measured simultaneously. In this experiment, the ions were not thermalized with buffer gas. Smaller shoulders can be seen, for example, at the C_7H_x^+ peak. This indicates that the peak is composed of ions with different numbers of hydrogen atoms. During collisional ionization, the norbornadiene molecule can fragment by loss of carbon and hydrogen atoms. In Fig. 7, it can be seen that the fragmentation yield is higher for the

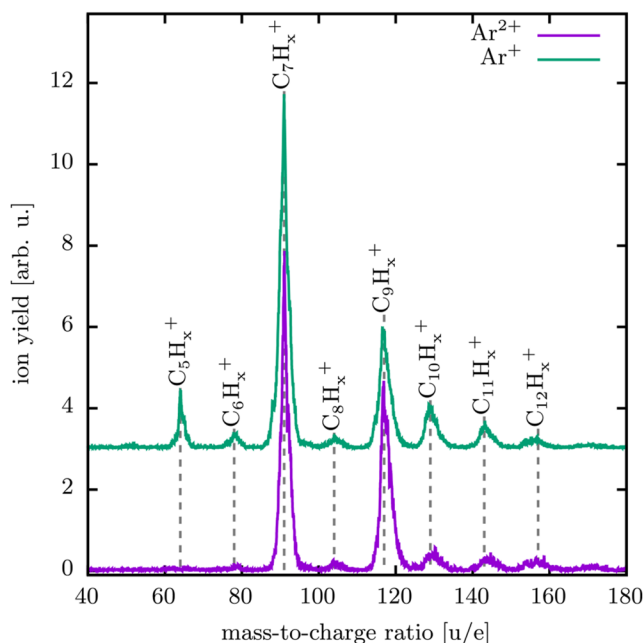
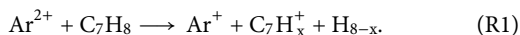


FIG. 7. The time-of-flight mass spectrum resulting from Ar^+ and Ar^{2+} impact ionization of norbornadiene, C_7H_8 . For better visibility, the ion yield of Ar^+ was offset by three arbitrary units. In addition to the single-ionization product C_7H_x^+ , ions with lower masses (fragments) and ions with higher masses (chemical-reaction compounds) can be seen. The mass spectra were obtained by summing up all recorded mass spectra over the total reaction time interval 0 to 40 ms.

impact ionization by Ar^+ compared to Ar^{2+} . Charge transfer from the Ar^{2+} ions to the target molecule occurs at a large impact parameter. As a consequence, there is only a small momentum transfer to the target molecule, and with this, the probability of the norbornadiene fragmentation is reduced. In the following, only the Ar^{2+} ion part with less fragmentation of the norbornadiene molecule will be discussed. The predominant collision process can be described by



Alternatively, one or several carbon atoms can be removed from the original target molecule. However, not only fragments are detected, but we also observe larger molecules, see Fig. 7. The largest peak is found for the C_9H_x^+ ion and products up to $\text{C}_{12}\text{H}_x^+$ are visible. Following the ionization, there is obviously the possibility that the generated ion reacts with a neutral norbornadiene molecule. During this reaction, acetylene, C_2H_2 , can be transferred from a neutral norbornadiene molecule to the initially generated ion according to the reaction

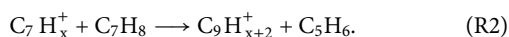


Figure 7 shows that the formation of C_9H_x^+ resulting from the ionization by Ar^{2+} is clearly preferred compared to the Ar^+ case. Another possible process would be that a charged $\text{C}_5\text{H}_{8-i}^+$ molecular ion and a neutral C_9H_{x+i} molecule are formed. However, from the mass spectrum in Fig. 7, it is obvious that this reaction plays only a minor role.

In Fig. 8, the generation of the C_7H_x^+ ions by Ar^{2+} ion-impact ionization and the production of C_9H_x^+ are shown, depending on the reaction time in the ion trap. In the first 12 ms, the Ar^{2+} ion beam passes through the trap and ionizes norbornadiene molecules according to Eq. (R1). After the opening time of PC I, t_{I} , in this case of 12 ms, the ion-trap entrance is closed again and the ion yield of C_7H_x^+ starts to decrease. Since some C_7H_x^+ ions are still present in the trap, together with neutral C_7H_8 gas, the production of $\text{C}_9\text{H}_{x+i}^+$ continues. This can be seen from the further increase in the reaction product according to Eq. (R2). After 30 ms, the amount of C_9H_x^+ in the trap stops increasing. The decrease of C_7H_x^+ can be described by a rate equation. There are two processes that affect the loss of ionized target ions C_7H_x^+ from the trap. Square brackets denote the spatial density of the ionized target molecules. One process is the spontaneous loss of the C_7H_x^+ ions, which is described by $k_{\text{trap}} \text{C}_7\text{H}_x^+ \cdot [\text{C}_7\text{H}_x^+]$. The other process is given by losses due to possible reactions, as described by Eq. (R2), which are represented by $k_{\text{reac}} \cdot [\text{C}_7\text{H}_8] \cdot [\text{C}_7\text{H}_x^+]$. Since there are significantly more neutral norbornadiene molecules than C_7H_x^+ ions in the trap, it can be assumed that only the proportion of trapped ions determines the rate of the reaction. For this reason, the gas pressure $[\text{C}_7\text{H}_8]$ and, therefore, the density of neutral molecules, which is independent of the measurement time, are unaccounted for in the further consideration, and reactions are described by $k_{\text{ps reac}} \cdot [\text{C}_7\text{H}_x^+]$. Hence, the reaction can be described by a pseudo-first-order process.^{22,41} The loss rate of the C_7H_x^+ density can be described by the rate equation

$$\frac{d[\text{C}_7\text{H}_x^+]}{dt} = -(k_{\text{trap}} \text{C}_7\text{H}_x^+ + k_{\text{ps reac}})[\text{C}_7\text{H}_x^+]. \quad (2)$$

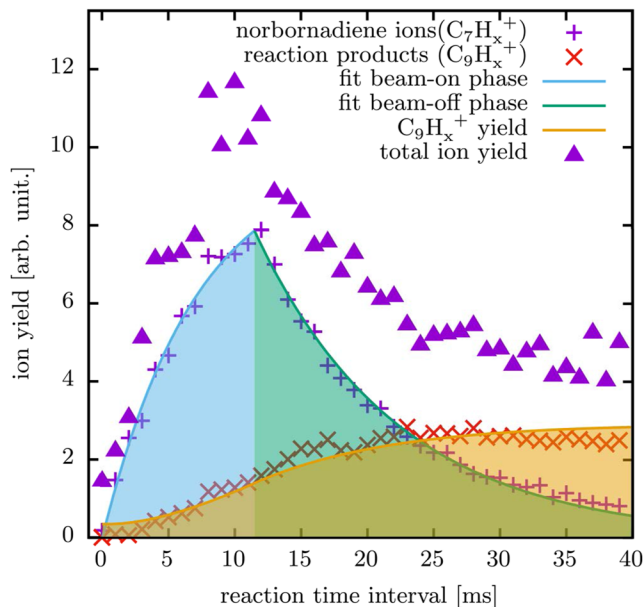


FIG. 8. Progression of the norbornadiene ion C_7H_x^+ yield generated by Ar^{2+} impact and the ion yield of the reaction product ion C_9H_x^+ as a function of time, measured by scanning the delay time t_{D} between opening PC I and PC II. The C_7H_x^+ ion yield was fitted with Eqs. (3) and (5). The time-dependent ion yield of the reaction product C_9H_x^+ is given by Eq. (7). It should be noted that the C_9H_x^+ curve depends on the evolution of the C_7H_x^+ reactant. The total ion yield shows that the norbornadiene ions and the reaction products make up far more than the largest part. The drop in the total ion yield is due to reactions to non-trappable reaction products, e.g., neutrals, H^+ or H_2^+ .

The solution of the differential Eq. (2) is an exponential function in t:

$$[\text{C}_7\text{H}_x^+] = A \cdot e^{-t/\tau}. \quad (3)$$

The characteristic time τ is given by $1/(k_{\text{trap}} \text{C}_7\text{H}_x^+ + k_{\text{ps reac}})$. In Fig. 8, this function was used to fit the measured decay of the C_7H_x^+ ion density as a function of time (resulting in the green curve). A value for τ of (10.5 ± 2) ms was determined, which represents a lower estimate for the trapping time. τ is relatively short, since the reactions take place in the trap, where the charge is transferred to light fragments such as H^+ or H_2^+ cations connected with larger neutral products. These very light ionic products cannot be further trapped and ion losses occur, which can be seen in the total ion yield (see Fig. 8).

In order to describe the C_7H_x^+ production phase, the rate Eq. (2) is supplemented by the term $k_{\text{ion}} \cdot [\text{C}_7\text{H}_8] \cdot [\text{Ar}^{2+}]$, where k_{ion} is the ionization probability per unit time. The ionizing properties and kinetic energy of the ion, as well as the ionizability of the neutral target and the norbornadiene pressure, are summarized in the factor $k_{\text{ps ion}}$,

$$\frac{d[\text{C}_7\text{H}_x^+]}{dt} = k_{\text{ps ion}} \cdot [\text{Ar}^{2+}] - (k_{\text{trap}} \text{C}_7\text{H}_x^+ + k_{\text{ps reac}})[\text{C}_7\text{H}_x^+]. \quad (4)$$

The solution of the differential Eq. (4) is

$$[C_7H_x^+] = A2(1 - e^{-t/\tau}), \quad (5)$$

where $A2$ is the saturation density of $C_7H_x^+$, reached after infinite exposure time and is given by the product of $k_{ps\ ion} \cdot [Ar^{2+}]$ and τ . In Fig. 8, this function was used to fit the measured build-up of $C_7H_x^+$ density during the first 12 ms (resulting in the blue curve).

The $C_9H_x^+$ reaction product can be described by the rate equation

$$\frac{d[C_9H_x^+]}{dt} = k_{ps\ reac\ C_9H_x^+} [C_7H_x^+] - k_{trap\ C_9H_x^+} [C_9H_x^+]. \quad (6)$$

The equation consists of two terms: The first term describes the formation of $C_9H_x^+$ through reactions as described by Eq. (R2), and the second term describes the trapping losses of $C_9H_x^+$. $k_{ps\ reac\ C_9H_x^+}$ is the reaction rate for the reaction shown in Eq. (R2). In contrast to $k_{ps\ reac}$, other reactions between $C_7H_x^+$ and C_7H_8 that lead to a different product are no longer included in $k_{ps\ reac\ C_9H_x^+}$. In principle, the $C_7H_x^+$ ions and C_7H_8 molecules could react to form other ionic products, as well as neutral products. The solution of the differential Eq. (6) is

$$[C_9H_x^+] = k_{ps\ reac\ C_9H_x^+} \cdot \int_0^t [C_7H_x^+] dt + A3 \cdot e^{-t/\tau_2}. \quad (7)$$

Since the time dependence of the $[C_7H_x^+]$ ion yield can be described by the fits with Eq. (3) for the range above 12 ms and Eq. (5) for the range 0 to 12 ms (see the green and blue curves and accordingly the areas below the curves in Fig. 8), the solution of the integral in Eq. (7) is known. Accordingly, $k_{ps\ reac\ C_9H_x^+}$, $A3$, and τ_2 can be fitted to the measured data. Here, τ_2 is equal to $1/k_{trap\ C_9H_x^+}$. The formation of $C_9H_x^+$, which is determined by the presence of norbornadiene ions, is described by the rate constant $k_{ps\ reac\ C_9H_x^+}$. From the fit to the measured yield of $C_9H_x^+$ ions, resulting in the yellow curve in Fig. 8, a value for $k_{ps\ reac\ C_9H_x^+}$ of about $20\ s^{-1}$ (corresponding to the characteristic time of 50 ms) is obtained at a norbornadiene pressure of $p = 1 \times 10^{-4}$ Pa. The pressure was measured in the high-vacuum chamber with a hot-cathode vacuum gauge. Since the gas inlet is directly pointing into the trap, the pressure in the trap is slightly higher than that in the high-vacuum chamber. The ion-gauge correction factor of 5.56 for toluene was used to correct the gas pressure.³⁴ The pressure results in a particle density of $2.4 \times 10^{10}\ cm^{-3}$. This corresponds to a reaction constant of $8 \times 10^{-10}\ cm^3\ s^{-1}$. The reaction constant $k_{ps\ reac\ C_9H_x^+}$ is limited by the assumption that we deal with a pseudo-first-order process^{22,41} here. Theoretically, this reaction can be described as a first approximation with the Langevin model.^{42,43} Since the required polarizability cannot be found in the literature, the analytical polarizability through coupled-perturbed self-consistent field calculations was used in the Langevin model. The calculations were performed in the quantum chemical program ORCA^{44,45} using the basis set def2-TZVPP and the functional B3LYP. The calculated polarizability of norbornadiene is $1.1 \times 10^{-23}\ cm^3$. The method was verified by the results of benzene and toluene calculations, giving proper values compared to the literature.⁴⁶ Using the polarizability of norbornadiene, a theoretical Langevin rate constant of $1.1 \times 10^{-9}\ cm^3\ s^{-1}$ could be calculated.

This Langevin rate constant has a slightly larger value than the one corresponding to the particle density, since the reactions between $C_7H_x^+$ and C_7H_8 to other products are contained in this.

Approximately, a value for τ_2 of 50 ms could be estimated. Since τ_2 clearly exceeds the measuring time of a cycle and since the decrease due to the trapping time is very small, it is not possible to determine τ_2 more precisely, and this can be regarded as a lower limit. The absence of reactive collisions between the $C_9H_x^+$ ions and the C_7H_8 molecules results in a much longer τ_2 . The observed time is the lower limit of the characteristic storage capability of the trap setup (see Fig. 8). The rate constants clearly show that it is possible to examine chemical reactions and their kinetics using our ion trap.

IV. CONCLUSION

We have introduced a new ion-trap setup and demonstrated its potential for studying a wide spectrum of reactions, illustrated by two exemplary experiments. The combination of the ion trap and the time-of-flight spectrometer, which has reached a mass resolution of $m/\Delta m = 242$ (see Table II), represents a powerful arrangement, which in combination with the remaining PIPE setup, allows for many experimental options. The time-of-flight spectrometer can analyze the mass-to-charge ratio of all trapped ions in 50 μs . It yields a very quick overview of all ions formed in the trap. The trapping characteristics of the ion trap are sufficient to detect ions with a mass-to-charge ratio of less than 20 u/e (see Xe^{7+} in Fig. 6). The low radio frequency of 3 MHz improves the trapping characteristics for higher mass-to-charge ratios. The trap should allow for larger molecular ions or charged nanoparticles with a mass-to-charge ratio of several 1000 u/e. In addition to the generation of ions directly in the trap, there is also the possibility to couple ions from the ion beamline into the radio-frequency potential. To enable this, a potential of up to 2000 V can be applied to the trap elements in order to reduce the kinetic energy of the ions to a few eV. With this option, ions of diverse sources, which can be installed on the high-voltage platform of PIPE, can be investigated with the ion-trap setup. In addition to photoexcitation and impact ionization, chemical reactions could be observed using the trap. Due to the high degree of integration into the existing PIPE setup, the ion trap offers many experimental possibilities that open up numerous new research fields.

ACKNOWLEDGMENTS

Parts of this research were carried out at the light source PETRA III at DESY, a member of the Helmholtz Association (HGF). We would like to thank M. Hoesch, J. Buck, F. Scholz, K. Bagschik, and J. Seltmann for their assistance in using beamline P04. Furthermore, we would like to thank J. Viehhaus (Helmholtz-Zentrum Berlin für Materialien und Energie, Germany), K. Baev, K. Schubert, S. Klumpp (Deutsches Elektronen-Synchrotron, Germany), and H. B. Pedersen (Aarhus University, Denmark), for the great cooperation. This project is funded by the Bundesministerium für Bildung und Forschung (BMBF) funding scheme (Grant Nos. 05K10RG1, 05K10GUB, 05K16RG1, 05K16GUC, and 05K19GU4), and by the Deutsche Forschungsgemeinschaft (DFG, German Research Foundation - Projects Nos. 245652604, 389115454, and 201267377). AG

acknowledges the Ministry of Science and Higher Education of Russia for the financial support (State assignment in the field of scientific activity, Grant No. 0852-2020-0019).

AUTHOR DECLARATIONS

Conflict of Interest

The authors have no conflicts to disclose.

Author Contributions

S. Reinwardt: Formal analysis (equal); Investigation (equal); Visualization (equal); Writing – original draft (equal); Writing – review & editing (equal). **I. Baev:** Investigation (equal); Writing – review & editing (equal). **F. Linß:** Investigation (equal). **P. Cieslik:** Investigation (equal). **O. Raberg:** Investigation (equal). **T. Buhr:** Investigation (equal). **A. Perry-Sassmannshausen:** Investigation (equal). **S. Schippers:** Investigation (equal); Writing – review & editing (equal). **A. Müller:** Investigation (equal); Writing – review & editing (equal). **F. Trinter:** Investigation (equal); Writing – review & editing (equal). **A. Guda:** Conceptualization (equal); Methodology (equal); Visualization (equal); Writing – review & editing (equal). **R. Laasch:** Conceptualization (equal); Investigation (equal). **M. Martins:** Conceptualization (equal); Funding acquisition (equal); Investigation (equal); Project administration (equal); Supervision (equal); Writing – original draft (equal); Writing – review & editing (equal).

DATA AVAILABILITY

The data that support the findings of this study are available from the corresponding author upon reasonable request.

REFERENCES

- ¹P. Sedigh Rahimabadi, M. Khodaei, and K. R. Koswattage, *X-Ray Spectrom.* **49**, 348 (2020).
- ²K. Ueda, E. Sokell, S. Schippers, F. Aumayr, H. Sadeghpour, J. Burgdörfer, C. Lemell, X.-M. Tong, T. Pfeifer, F. Calegari, A. Palacios, F. Martin, P. Corkum, G. Sansone, E. V. Gryzlova, A. N. Grum-Grzhimailo, M. N. Piancastelli, P. M. Weber, T. Steinle, K. Amini, J. Biegert, N. Berrah, E. Kukk, R. Santra, A. Müller, D. Dowek, R. R. Lucchese, C. W. McCurdy, P. Bolognesi, L. Avaldi, T. Jahnke, M. S. Schöffler, R. Dörner, Y. Mairesse, L. Nahon, O. Smirnova, T. Schlathöler, E. E. B. Campbell, J.-M. Rost, M. Meyer, and K. A. Tanaka, *J. Phys. B: At. Mol. Opt. Phys.* **52**, 171001 (2019).
- ³R. Lindblad, L. Kjellsson, R. C. Couto, M. Timm, C. Bülow, V. Zamudio-Bayer, M. Lundberg, B. von Issendorff, J. T. Lau, S. L. Sorensen, V. Carravetta, H. Ågren, and J.-E. Rubensson, *Phys. Rev. Lett.* **124**, 203001 (2020).
- ⁴S. Bari, L. Inhester, K. Schubert, K. Mertens, J. O. Schunck, S. Dörner, S. Deinert, L. Schwob, S. Schippers, A. Müller, S. Klumpp, and M. Martins, *Phys. Chem. Chem. Phys.* **21**, 16505–16514 (2019).
- ⁵J.-P. Mosnier, E. T. Kennedy, P. van Kampen, D. Cubaynes, S. Guilbaud, N. Sisourat, A. Puglisi, S. Carniato, and J.-M. Bizau, *Phys. Rev. A* **93**, 061401(R) (2016).
- ⁶M. Martins, S. Reinwardt, J. O. Schunck, J. Schwarz, K. Baev, A. Müller, T. Buhr, A. Perry-Sassmannshausen, S. Klumpp, and S. Schippers, *J. Phys. Chem. Lett.* **12**, 1390 (2021).
- ⁷J. T. Lau, J. Rittmann, V. Zamudio-Bayer, M. Vogel, K. Hirsch, P. Klar, F. Lofink, T. Möller, and B. von Issendorff, *Phys. Rev. Lett.* **101**, 153401 (2008).
- ⁸B. A. McGuire, *Astrophys. J. Suppl. Ser.* **259**, 30 (2022).

- ⁹I. C. Lyon, B. Peart, J. B. West, and K. Dolder, *J. Phys. B: At. Mol. Phys.* **19**, 4137 (1986).
- ¹⁰H. Kjeldsen, *J. Phys. B: At. Mol. Opt. Phys.* **39**, R325 (2006).
- ¹¹S. Schippers, A. L. D. Kilcoyne, R. A. Phaneuf, and A. Müller, *Contemp. Phys.* **57**, 215 (2015).
- ¹²R. Thissen, J. M. Bizau, C. Blancard, M. Coreno, C. Dehon, P. Franceschi, A. Giuliani, J. Lemaire, and C. Nicolas, *Phys. Rev. Lett.* **100**, 223001 (2008).
- ¹³S. Schippers, S. Ricz, T. Buhr, A. Borovik, Jr., J. Hellhund, K. Holste, K. Huber, H.-J. Schäfer, D. Schury, S. Klumpp, K. Mertens, M. Martins, R. Flesch, G. Ulrich, E. Rühl, T. Jahnke, J. Lower, D. Metz, L. P. H. Schmidt, M. Schöffler, J. B. Williams, L. Glaser, F. Scholz, J. Seltmann, J. Viehhaus, A. Dorn, A. Wolf, J. Ullrich, and A. Müller, *J. Phys. B: At. Mol. Opt. Phys.* **47**, 115602 (2014).
- ¹⁴S. Schippers, A. Borovik, Jr., T. Buhr, J. Hellhund, K. Holste, A. L. D. Kilcoyne, S. Klumpp, M. Martins, A. Müller, S. Ricz, and S. Fritzsche, *J. Phys. B: At. Mol. Opt. Phys.* **48**, 144003 (2015).
- ¹⁵A. Müller, A. Borovik, Jr., S. Bari, T. Buhr, K. Holste, M. Martins, A. Perry-Sassmannshausen, R. A. Phaneuf, S. Reinwardt, S. Ricz, K. Schubert, and S. Schippers, *Phys. Rev. Lett.* **120**, 133202 (2018).
- ¹⁶A. Müller, M. Martins, A. Borovik, Jr., T. Buhr, A. Perry-Sassmannshausen, S. Reinwardt, F. Trinter, S. Schippers, S. Fritzsche, and A. S. Kheifets, *Phys. Rev. A* **104**, 033105 (2021).
- ¹⁷S. Klumpp, A. A. Guda, K. Schubert, K. Mertens, J. Hellhund, A. Müller, S. Schippers, S. Bari, and M. Martins, *Phys. Rev. A* **97**, 033401 (2018).
- ¹⁸S. W. Epp, J. R. Crespo López-Urrutia, G. Brenner, V. Mäckel, P. H. Mokler, R. Treusch, M. Kuhlmann, M. V. Yurkov, J. Feldhaus, J. R. Schneider, M. Wellhöfer, M. Martins, W. Wurth, and J. Ullrich, *Phys. Rev. Lett.* **98**, 183001 (2007).
- ¹⁹J. Martens, G. Berden, C. R. Gebhardt, and J. Oomens, *Rev. Sci. Instrum.* **87**, 103108 (2016).
- ²⁰D. Gerlich and S. Horning, *Chem. Rev.* **92**, 1509 (1992).
- ²¹M. Tomza, K. Jachymski, R. Gerritsma, A. Negretti, T. Calarco, Z. Idziaszek, and P. S. Julienne, *Rev. Mod. Phys.* **91**, 035001 (2019).
- ²²O. A. Krohn, K. J. Catani, and H. J. Lewandowski, *Phys. Rev. A* **105**, L020801 (2022).
- ²³N. S. Holmes, *Atmos. Environ.* **41**, 2183 (2007).
- ²⁴R. Teiwes, J. Elm, K. Handrup, E. P. Jensen, M. Bilde, and H. B. Pedersen, *Phys. Chem. Chem. Phys.* **20**, 28606 (2018).
- ²⁵J. Viehhaus, F. Scholz, S. Deinert, L. Glaser, M. Ilchen, J. Seltmann, P. Walter, and F. Siewert, *Nucl. Instrum. Methods Phys. Res., Sect. A* **710**, 151 (2013).
- ²⁶A. Müller, D. Bernhardt, A. Borovik, Jr., T. Buhr, J. Hellhund, K. Holste, A. L. D. Kilcoyne, S. Klumpp, M. Martins, S. Ricz, J. Seltmann, J. Viehhaus, and S. Schippers, *Astrophys. J.* **836**, 166 (2017).
- ²⁷D. Gerlich and G. Kaefer, *Astrophys. J.* **347**, 849 (1989).
- ²⁸A. Svendsen, L. Lammich, J. E. Andersen, H. K. Bechtold, E. Søndergaard, F. Mikkelsen, and H. B. Pedersen, *Phys. Rev. A* **87**, 043410 (2013).
- ²⁹K. Geistlinger, M. Fischer, S. Spieler, L. Remmers, F. Duensing, F. Dahlmann, E. Endres, and R. Wester, *Rev. Sci. Instrum.* **92**, 023204 (2021).
- ³⁰R. Wester, *J. Phys. B: At. Mol. Opt. Phys.* **42**, 154001 (2009).
- ³¹SIMION, Version 8.1.1.32, Scientific Instruments Services, Inc., Ringoes, NJ, USA.
- ³²D. Gerlich, “Inhomogeneous RF fields: A versatile tool for the study of processes with slow ions,” in *Advances in Chemical Physics* (John Wiley & Sons, Ltd., 1992), pp. 1–176.
- ³³I. Cermak, *Rev. Sci. Instrum.* **76**, 063302 (2005).
- ³⁴J. E. Bartmess and R. M. Georgiadis, *Vacuum* **33**, 149 (1983).
- ³⁵O. Yagci and J. E. Wilson, *J. Phys. C: Solid State Phys.* **16**, 383 (1983).
- ³⁶N. Saito and I. H. Suzuki, *Int. J. Mass Spectrom.* **115**, 157 (1992).
- ³⁷N. Saito and I. H. Suzuki, *J. Phys. B: At. Mol. Opt. Phys.* **25**, 1785 (1992).
- ³⁸M. Krems, J. Zirbel, M. Thomason, and R. D. DuBois, *Rev. Sci. Instrum.* **76**, 093305 (2005).
- ³⁹T. R. Evans, *J. Am. Chem. Soc.* **93**, 2081 (1971).

⁴⁰I. Tabushi, K. Yamamura, Z.-i. Yoshida, and A. Togashi, *Bull. Chem. Soc. Jpn.* **48**, 2922 (1975).

⁴¹G. Innorta, L. Pontoni, and S. Torrioni, *J. Am. Soc. Mass Spectrom.* **9**, 314 (1998).

⁴²M. P. Langevin, *Ann. Chim. Phys.* **8**, 245 (1905).

⁴³G. Gioumousis and D. P. Stevenson, *J. Chem. Phys.* **29**, 294 (1958).

⁴⁴F. Neese, *Wiley Interdiscip. Rev.: Comput. Mol. Sci.* **2**, 73 (2012).

⁴⁵F. Neese, *Wiley Interdiscip. Rev.: Comput. Mol. Sci.* **8**, e1327 (2018).

⁴⁶M. Gussoni, M. Rui, and G. Zerbi, *J. Mol. Struct.* **447**, 163 (1998).